

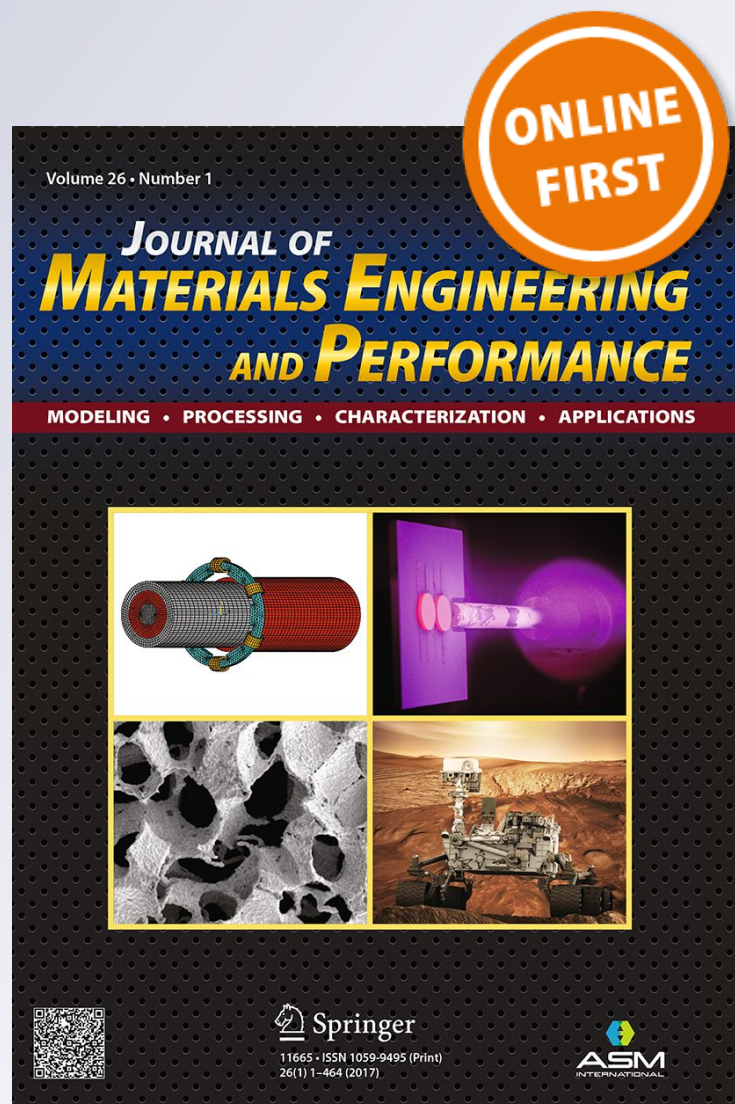
Alternative PWHT to Improve High-Temperature Mechanical Properties of Advanced 9Cr Steel Welds

Ariel Burgos, Hernán Svoboda, Zhuyao Zhang & Estela Surian

Journal of Materials Engineering and Performance


ISSN 1059-9495

J. of Materi Eng and Perform
DOI 10.1007/s11665-018-3736-5



Your article is protected by copyright and all rights are held exclusively by ASM International. This e-offprint is for personal use only and shall not be self-archived in electronic repositories. If you wish to self-archive your article, please use the accepted manuscript version for posting on your own website. You may further deposit the accepted manuscript version in any repository, provided it is only made publicly available 12 months after official publication or later and provided acknowledgement is given to the original source of publication and a link is inserted to the published article on Springer's website. The link must be accompanied by the following text: "The final publication is available at link.springer.com".

Alternative PWHT to Improve High-Temperature Mechanical Properties of Advanced 9Cr Steel Welds

Ariel Burgos , Hernán Svoboda, Zhuyao Zhang, and Estela Surian

(Submitted October 2, 2017; in revised form October 19, 2018)

Creep-resistant 9Cr steels are extremely important in thermal power generation industry due to their marked resistance to creep and corrosion. The weldability of these alloys is critical since they are used in welded construction equipment. The required mechanical properties are achieved after post-weld heat treatment. This study examined the effect of different post-weld heat treatments on microstructure and mechanical properties of creep strength-enhanced 9Cr steel welding deposits. It was obtained with an experimental flux-cored arc welding wire used under protective gas (Ar-20% CO₂). The heat treatments used were: (1) tempering (760 °C × 2 h), (2) solubilizing (1050 °C × 1 h) + tempering (760 °C × 2 h) and (3) solubilizing (1150 °C × 1 h) + first tempering (660 °C × 3 h) + second tempering (660 °C × 3 h). All-weld metal chemical composition was analyzed, and hot tensile tests were carried out at different temperatures. Charpy-V impact tests and Vickers microhardness measurements were also performed. Microstructures were studied using x-ray diffraction and optical and scanning electron microscopy. In all cases, a martensitic matrix with intergranular and intra-granular precipitates was detected. In the as-welded condition, δ -ferrite was also found. Microhardness dropped, and the impact energy increased with post-weld heat treatments. The highest hot tensile strength result was achieved with samples submitted to austenization at 1150 °C and double tempering at 660 °C.

Keywords creep strength-enhanced 9Cr steel, FCAW, mechanical properties, microstructure, PWHT

1. Introduction

The challenge for the new plants of thermal power generation is to increase both working temperature and steam pressure to be able to increase their efficiency, thus reducing the cost of combustible and the CO₂ emission into the environment. For a working temperature in the range of 600-650 °C and pressure of 30-35 MPa or more in service, the use of creep-resistant steels is required. A great advance in this field is the development of new creep-resistant 9Cr steels (Ref 1) in which B, Co and W are added; this last element replaced part of the original Mo content. These steels present good thermal conductivity and low linear thermal expansion coefficient that, together with their lower cost of fabrication and transformation to tubes, make them a good alternative for the construction of high thickness components (Ref 2, 3). In this context, the weldability of these steels is crucial. In recent times, the use of flux-cored arc welding (FCAW) consumables for this application has been improved replacing gas metal arc welding

(GMAW) solid wires and metal manual electrodes, because the fabrication of this type of equipment involves out-of-position weldments (e.g., overhead; vertical down and vertical up) (Ref 4-7). Since these steels are used in service at high temperatures (500-650 °C), toughness is not a problem because at this temperature range the risk of brittle fracture does not exist. Nevertheless, the welded joints must satisfy certain toughness requirements at room temperature during construction, hydrostatic testing or start-up. Consequently, there must be a compromise between toughness at room temperature and mechanical properties at high temperature (Ref 6-11). ISO 5380:2010 standard (Ref 12) requires, for this type of welding deposits, an average value of 47 J of absorbed energy in the Charpy-V impact test at room temperature (individual minimum value 38 J).

The development of consumables for welding of these new 9Cr steels has accompanied their development; however, further improvements are still required. The post-weld heat treatment (PWHT) is mandatory for these deposits to achieve the necessary final properties in the weldment. Hence, it is necessary to apply a PWHT which provides a pre-service microstructure with enough stability at the working temperature to delay the material degradation in the long term. The precipitates finely dispersed in the martensitic matrix (precipitation hardening) and the density of dislocations (dislocation hardening) mostly control the mentioned degradation together with the solid solution hardening effect provided by Mo and W contents (Ref 13). The creep strength-enhanced 9Cr steel (CSE9CrS) welding deposits show a martensitic structure with precipitates in the prior austenite grain boundaries, sub-boundaries and within sub-grains (M₂₃C₆ and MX); it is also possible to find δ -ferrite formed during the welding process, which was not transformed during cooling (Ref 2, 14, 15). The δ -ferrite in the final microstructure has a detrimental effect on toughness and on high-temperature properties (Ref 2). The

Ariel Burgos, School of Engineering, National University of Lomas de Zamora, Lomas de Zamora, Buenos Aires, Argentina; **Hernán Svoboda**, Materials and Structures Laboratory, INTECIN, School of Engineering, University of Buenos Aires, Buenos Aires, Argentina; and National Council of Scientific and Technical Research, Buenos Aires, Argentina; **Zhuyao Zhang**, Metrode Products Ltd., Chertsey, Surrey, UK; and **Estela Surian**, Argentine Siderurgy Institute, Buenos Aires, Argentina. Contact e-mail: arielburgo@gmail.com.

PWHT has the objective of tempering the welded joint structure when it is submitted to temperatures below AC1 promoting the formation of the mentioned precipitates: the δ -ferrite remains present.

Unlike the practice for weldments, the conventional heat treatments applied to the as-cast steels comprise an austenization at temperature above AC3 during which a homogenization of the chemical composition is produced together with the carbonitride (CN) dissolution, followed by an air/water cooling, resulting in a microstructure completely martensitic (Ref 16). Subsequently, the mentioned microstructure is tempered at temperatures below AC1 (Ref 16). There are studies where alternative heat treatments for these CSE9CrSs have been developed with success, resulting in an improvement in their properties during service: for example, increasing the austenization temperature and decreasing the tempering temperature, making a double tempering for longer times (Ref 16).

Nowadays, consumables matching the chemical composition of the steels have been developed and, in the literature, there are not many systematic studies using FCAW wires of last generation for these steels. Moreover, there is only scarce information about alternative PWHT for this type of deposits.

The objective of this work is to study the effect of conventional and alternative PWHTs on microstructure and mechanical properties of a FCAW-G CSE9CrS AWM. In this article, the deposit from the consumable without dilution with the base metal will be always referred as AWM. The microstructure was evaluated by optical microscopy (OM), scanning electron microscopy (SEM) and x-ray diffraction (XRD). Hardness and toughness at room temperature and tensile properties at high temperature by means of hot tensile

test (HTT) at different strain rates were measured. According to the literature (Ref 17-19), a relationship between HTT and creep resistance tests (CRT) can be established, as an approach to evaluate the service performance of the material.

2. Experimental Procedure

2.1 Weldments

An CSE9CrS AWM-coupon was welded according to ANSI/AWS A5.29/A5.29M: 2010 standard (Ref 20) with a flux-cored 1.2 mm diameter wire under shielding gas of Ar-20%CO₂. Buttering was performed with the same consumable. The welds were made with DC+, in flat position, with a gas flow rate of 20 L/min and a stick out of 12-15 mm, as shown in Fig. 1.

The pre-heat and interpass temperatures were 240 °C (± 10 °C). Average welding current were 223 A, voltage of 30.6 V, speed of 5.7 mm/s and heat input of 1.2 kJ/mm for 11 welding beads distributed in five layers.

The AWM was submitted to the radiographic test. Transversal cuts were extracted for macrographic study.

2.2 Chemical Composition

From the AWM-coupon, transversal cuts were extracted for chemical analysis, which was determined by optical emission spectrometry in the central zone corresponding to all-weld metal.

2.3 Post-Weld Heat Treatment

Conventional PWHT for steels of the type ASTM A213/A213M-15c:2015 (Ref 21) and A335/A335M-15a:2015 (Ref 22) standards (sample 76) and alternative PWHT (samples 176 and 166) were carried out. The last two ones had the objective of achieving a microstructure with both higher dislocation density and higher volume fraction of finer dispersion MX precipitates. The alternative PWHTs used here were previously applied in steels ASTM A213/A335 grade T/P92 base metal by Yin et al. (Ref 16). The PWHTs are shown in Table 1.

2.4 Microstructure

2.4.1 Optical and Scanning Electron Microscopy. A transversal cut of the welded coupon was prepared for the macroscopic analysis.

In the as-welded (AW) condition, δ -ferrite content was quantified according to ASTM E-562-02 standard (Ref 22) in a parallel cut to the fracture surface, in the longitudinal direction of the welding of the Charpy-V specimen. Twenty-two fields

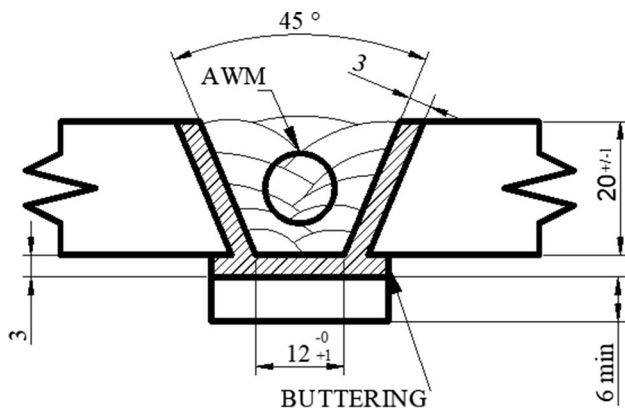


Fig. 1 ANSI/AWS A5.29/A5.29M:2010 coupon transversal cut. Dimensions in mm

Table 1 Sample identification and PWHT

PWHT	Solubilization		Tempering		Double tempering	
	Temperature, °C	Time, h	Temperature, °C	Time, h	Temperature, °C	Time, h
AW
76	760	2
176	1050	1	760	2
166	1150	1	660	3	660	3

AW, as-welded

were quantified using photomicrographs with 200× magnification.

2.4.2 X-ray Diffraction. Samples from the center of the AWM were extracted and analyzed by XRD, using a Cu anode with $\lambda = 1.548 \text{ \AA}$, in a range of diffraction angle $2\theta = 30^\circ\text{--}90^\circ$, applying a step of 0.02° and $0.5^\circ/\text{min}$ of speed.

2.5 Mechanical Properties

2.5.1 Microhardness. On the AW samples prepared for macrographic analysis, Vickers microhardness measurements (HV1000) on every 0.5 mm were performed on four lines (Fig. 2): The horizontal one covered all the beds of the fifth layer and the three vertical ones covered all the passes. The different zones of the welded joint were identified.

On the other hand, on a sample extracted from AWM after post-weld treatment, HV1000 hardness was measured in a 5 mm^2 (center and four vertices). The representative value of this area was determined as an average of these measurements.

2.5.2 Hot Tensile Tests. Transversal tensile specimens were machined according to ASTM E 8 M-01 standard (Ref 22), Fig. 3(a). They were submitted to HTTs at $600 \text{ }^\circ\text{C}$ with the initial strain rates of $2.67\text{E}\text{--}05$, $1.33\text{E}\text{--}04$, $1.33\text{E}\text{--}03$ and $6.67\text{E}\text{--}03 \text{ 1/s}$.

2.5.3 Charpy-V Impact Tests. Charpy-V specimens were extracted according to AWS A5.29/A5.29M:2010 standard (Ref 20). They were machined according to ASTM E23-02a—Type A (Ref 23) Fig. 3(b). For each condition studied,

two samples were tested at $20 \text{ }^\circ\text{C}$; the results were averaged.

3. Results and Discussion

3.1 Welds

Figure 4 shows a transversal cut of an AWM-coupon. According to AWS A5.29/A5.29M:2010 standard (Ref 20), very low level of defects was detected as it was shown in the radiographic test performed.

3.2 All-Weld Metal Chemical Composition

The AWM chemical composition obtained on the last bead in weight percent was 9.33Cr, 1.89W, 0.51Mo, 0.21V, 0.05Nb, 0.36Si, 0.90Mn, 0.12C, 0.017P, 0.007S, 0.49Ni, 0.052N, 0.86Co, 0.08Cu, 0.001Al, 0.03Ti, 0.002B and Fe balance.

Chemical composition is in accordance with a commercial welding electrode type T/P92 with the B content restricted to 0.002%. Some Ti content was detected which is associated to the rutile (titanium oxide) used for the formation of the protective slag in the FCAW-G process. In contrast, the Co content is added to stabilize the austenite and to avoid the formation of δ -ferrite during solidification, improving the tensile strength and toughness at room temperature (Ref 24). The combination of Mn and Ni tends to diminish the AC1 critical temperature. The PWHT temperature has to be near but below AC1. Nevertheless, it is important that no partial transformation to austenite could be produced during PWHT. In this sense, the restriction of Mn + Ni to 1.5% weight maximum is usually imposed (Ref 20).

3.3 Microstructure

Figure 5 and 6 present micrographs of AW samples in different multipass joint locations. A martensitic matrix with δ -ferrite was detected.

In the last bead, it could be observed a typical columnar martensitic structure of directional solidification. The martensitic structure is obtained even at low cooling velocities for formation of austenite (Ref 25), with some blocks of intergranular δ -ferrite, as shown in Fig. 5(a). This last phase was retained during cooling and persisted after the reheating produced by the following bead, as shown in Fig. 5(b). This fact could be explained considering a local enrichment in Cr and Mo (due to the dissolution of M_{23}C_6 , which are rich in Cr),

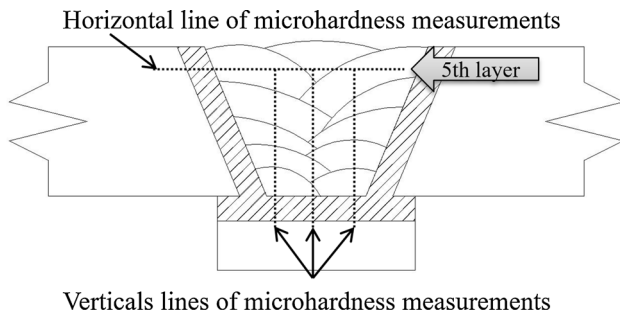


Fig. 2 Location of HV1000 measurements

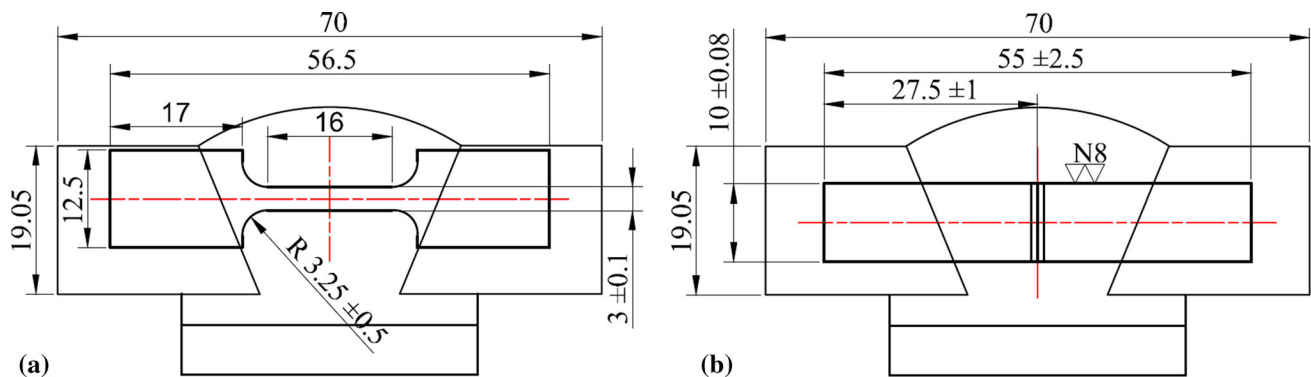


Fig. 3 (a) Transversal tensile specimen location. Dimension in mm. (b) Charpy-V specimen location. Dimension in mm

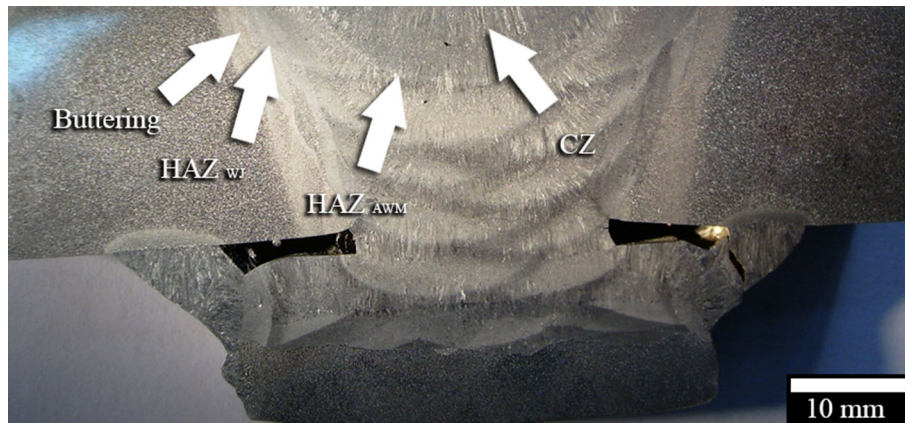


Fig. 4 Photomicrograph of the multipass all-weld metal coupon (Vilella reagent). CZ—Columnar zone; HAZ_{AWM}—Heat-affected zone all-weld metal; HAZ_{wj}—Heat-affected zone welding joint

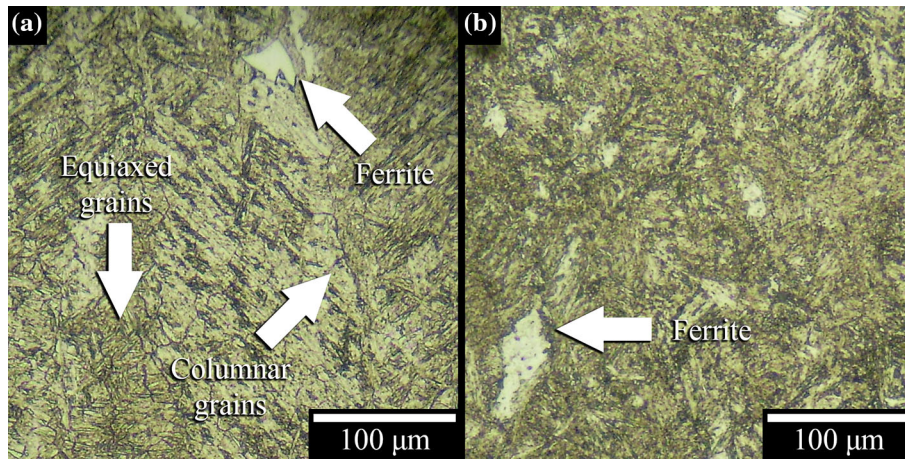


Fig. 5 OM micrographs of samples AW in different positions of the multipass joint. (a) 5° layer: fusion zone (FZ); FL; HAZ_{AWM}, (b) 3° layer: HAZ_{AWM}

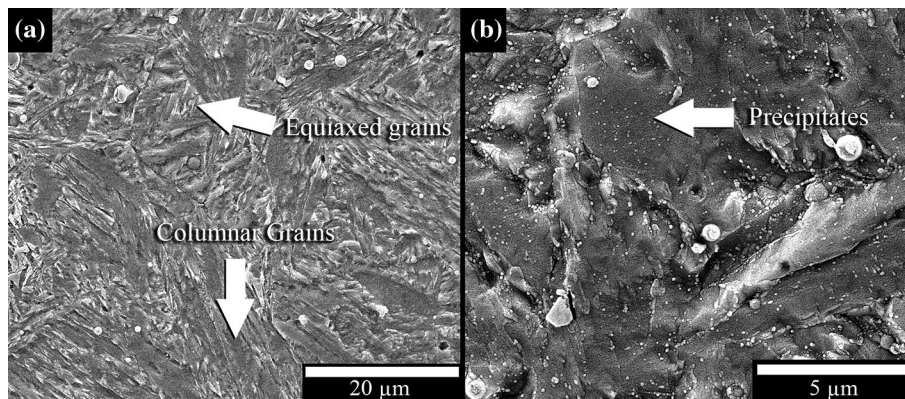


Fig. 6 SEM micrographs of AW samples: (a) matrix: mixed structure (columnar grains and equiaxed grain), (b) HAZ_{AWM}: precipitates

along the prior austenitic grain boundary. These segregated areas enriched of these ferrite stabilizer elements present preferential sites for the δ -ferrite nucleation (Ref 26). The results from the manual counting indicated that the AW samples had 2.3% (\pm 1.6%) of δ -ferrite.

Below the fusion line (FL) of any bead of the multipass joint, in the heat affect zone (HAZ_{AWM}), Fig. 5(a) and 6(a), it was possible to observe how the columnar grains collapsed

and an equiaxial grain structure developed. This fact was produced due to the temperature interval to which this zone was exposed by the following bead (Ref 10). In the HAZ_{AWM}, far from the FL, because of the thermal cycles generated by the subsequent passes, intercritical ($AC1 < T < AC3$) and subcritical ($T < AC1$) temperatures could be reached. Because of this, it could be observed a higher quantity of precipitates, Fig. 6(b) (Ref 25). According to (Ref

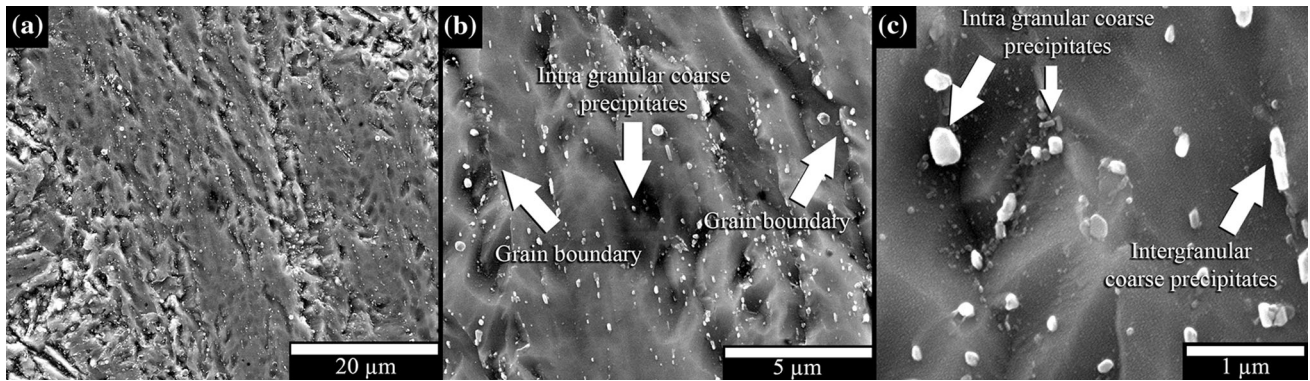


Fig. 7 SEM micrographs of 76 sample (a) matrix: mixed structure with precipitates (b) matrix: grain boundary (c) matrix: different precipitates

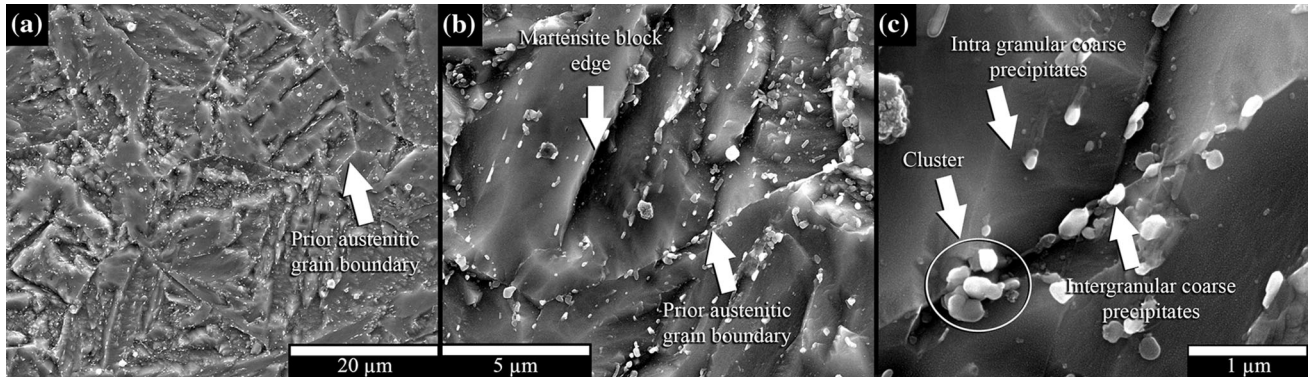


Fig. 8 SEM micrographs of 176 sample (a) and (b) matrix: equiaxed structure with precipitates (c) different precipitates

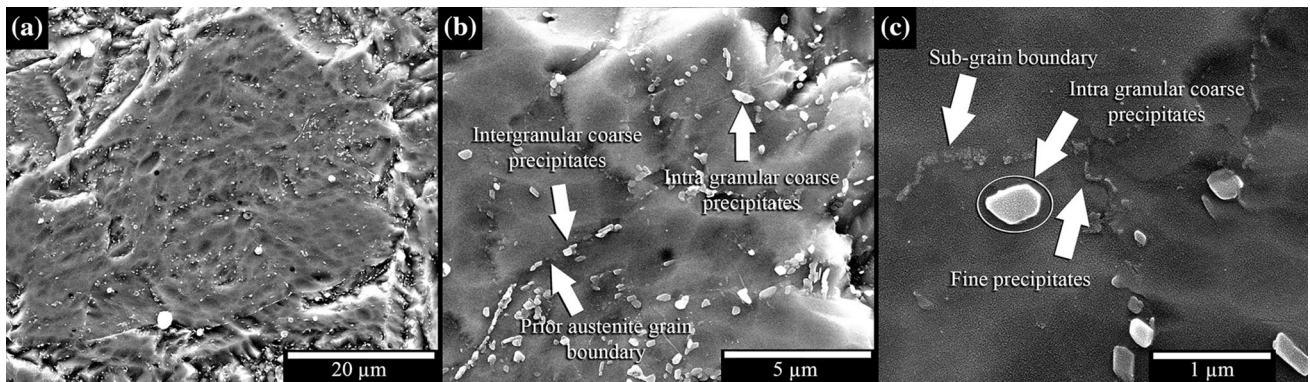


Fig. 9 SEM micrographs of 166 sample (a) and (b) matrix: equiaxed structure of primary grains and sub-grains with precipitates (c) different precipitates; sub-grain boundary identification

10, 27), they could be of the types $M_{23}C_6$ and MX. δ -ferrite was not found in PWHT samples.

Sample 76 submitted to a simple tempering showed a mixed microstructure of columnar and equiaxial grains with both inter- and intra-granular precipitates (Fig. 7). On the other hand, in solubilized samples (176 and 166) the columnar structure was eliminated, showing an equiaxed microstructure with more homogeneous grains of increased size, with both inter- and intra-granular precipitates (Fig. 8 and 9).

Sample 166, which reached higher solubilizing temperature than sample 176, showed higher prior austenitic grain size (Fig. 9a) than sample 176, and as a consequence a more

homogeneous precipitate distribution (Fig. 9a compared to Fig. 8a). In this last figure, it was possible to notice that there was high quantity of precipitates in the prior austenitic grain boundary, showing some clusters (Fig. 8c) compared to those found in the martensite lath of sample 166 (Fig. 9b).

The coarse precipitates located at the prior austenitic grain boundary and the lath of martensite could be $M_{23}C_6$ according to the literature (Ref 14, 28-30). They present a complex composition $(Fe,Cr,W,Mo)_{23}C_6$ and tend to grow easily with the service temperature (Ref 14, 28-30). The fine precipitates located at the edge of the martensite lath could be MX (Ref 14, 28-30). On the contrary, MX precipitates, much smaller than $M_{23}C_6$, are

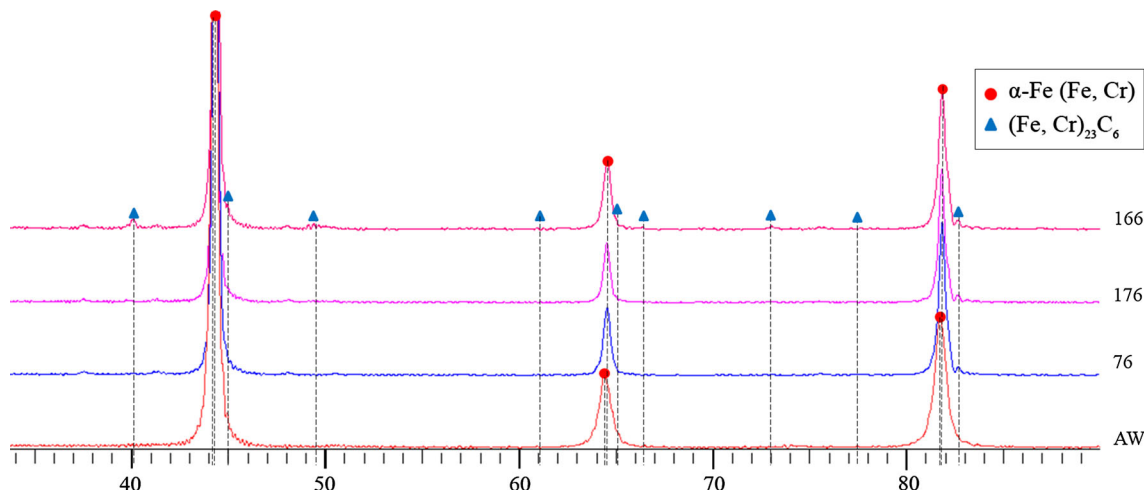


Fig. 10 XRD patterns for different PWHT

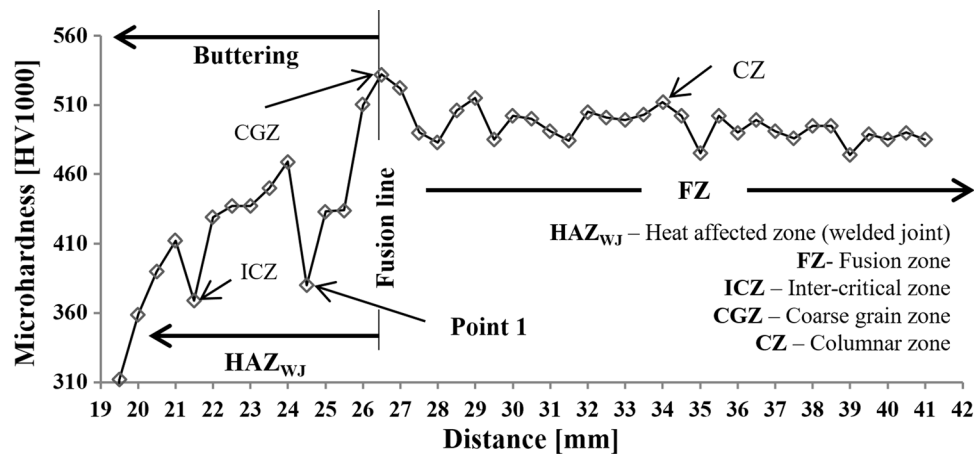


Fig. 11 HV1000 microhardness of AW sample of horizontal line on multipass joint (5° layer)

composed by $M = (V, Nb, Cr)$ and $X = (C, N)$ and their growth is slow (Ref 14, 28-30). Figure 8(c) and 9(c) show different types of precipitates found in samples 176 and 166, respectively. The smallest precipitates MX were supposed to be responsible for the good behavior that this alloy system presents at high temperature (Ref 31, 32). It can also be noticed that in sample 166 sub-grains are formed inside the martensite laths.

In Fig. 10, XRD patterns are presented. They were mainly peaks in the planes (110), (200) and (211), belonging to the matrix (α -Fe). It can be observed that with the PWHT the peaks were slightly displaced to higher angles regarding the AW sample. This fact could indicate that alloying elements (as Cr, Mo, W) previously in solid solution have precipitated as carbides $M_{23}C_6$, impoverishing the matrix (Ref 33, 34). As it can be noticed, some peaks corresponding to these carbides started to appear with the different tempering treatments.

3.4 Mechanical Properties

3.4.1 Microhardness. In Fig. 11, the results of HV1000 determination are presented for the AW sample. Maximum values corresponded to zones which were just beyond the FL,

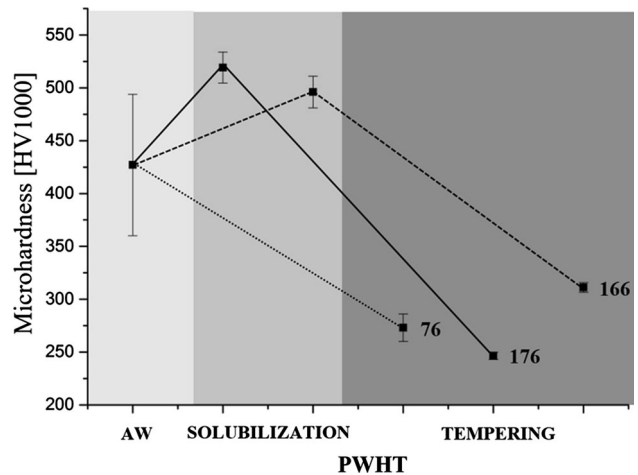


Fig. 12 Effect of PWHT on microhardness HV1000

where the material entered a biphasic field (δ ferrite + austenite), in the coarse grain HAZ_{AWM} . The achieved microstructure was martensite with carbides and retained δ -ferrite. The

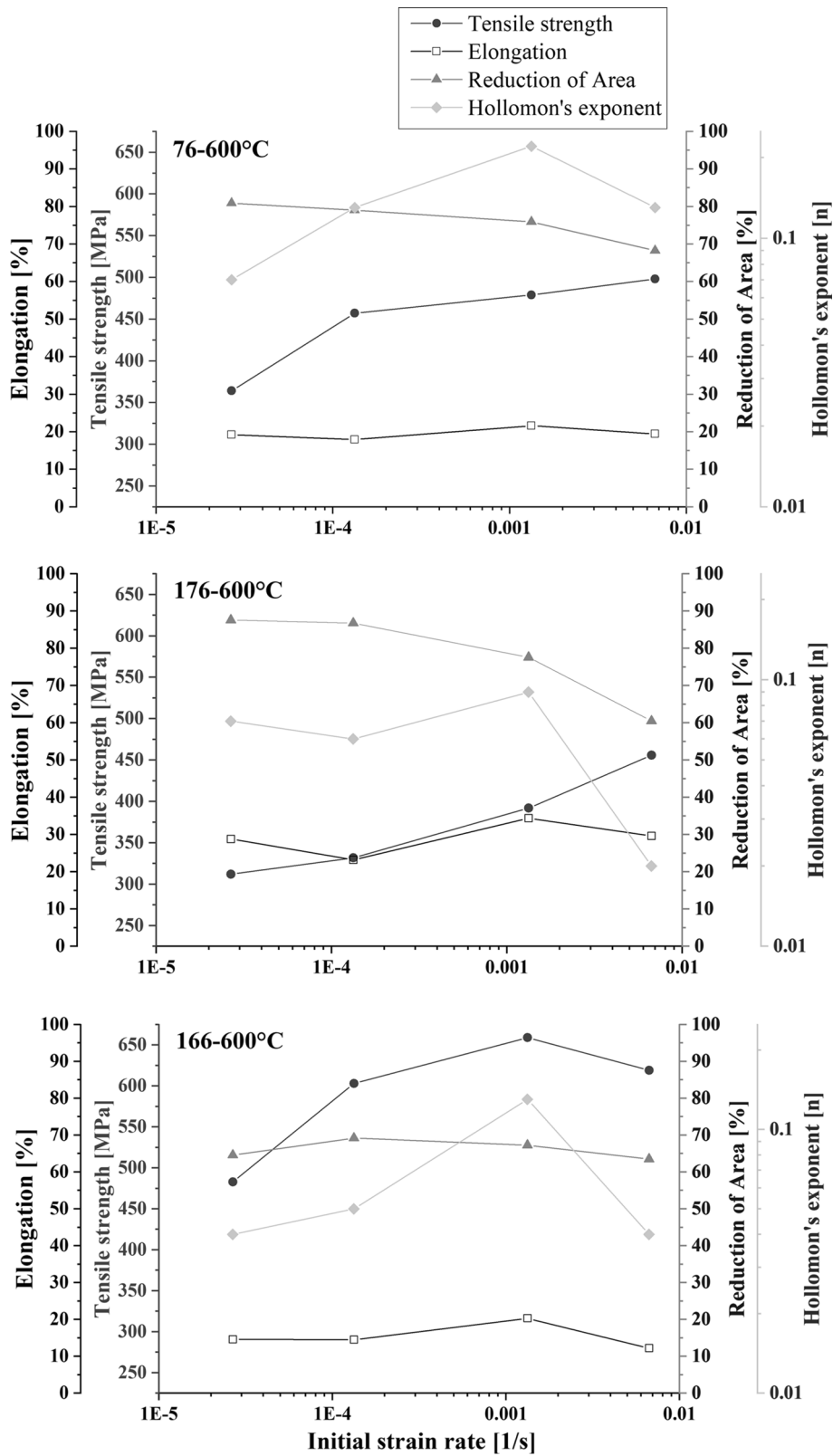


Fig. 13 The effect of the initial strain rate on the mechanical properties in HTT at 600 °C and the strain hardening exponent (n) of the Hollomon equation

Table 2 Mechanical properties at high temperatures and the Larson–Miller parameterization calculated from all PWHT

PWHT	Tensile strength σ_{UTS} , MPa	Time (σ_{UTS}) t , min	Larson–Miller parameter ($C = 30$)
76	364	48.71	31.4
	457	10.80	30.8
	479	3.50	30.4
	498	0.15	29.2
176	312	32.50	31.2
	332	5.87	30.6
	392	0.83	29.8
	456	0.26	29.4
166	483	30.99	31.2
	603	4.99	30.5
	659	0.91	29.8
	619	0.12	29.1

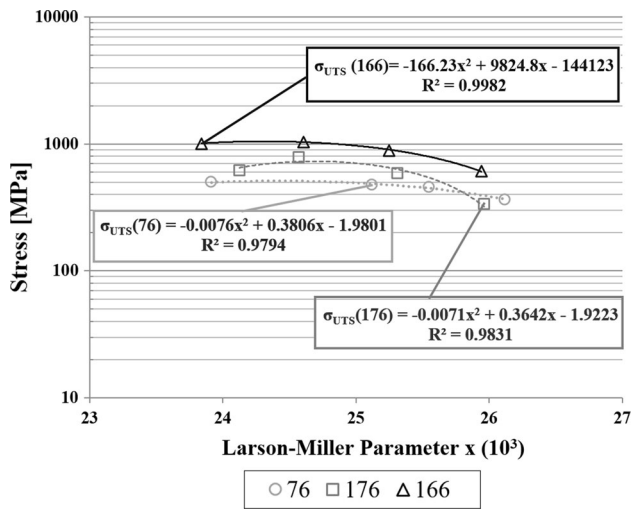


Fig. 14 Larson–Miller plot for different PWHT

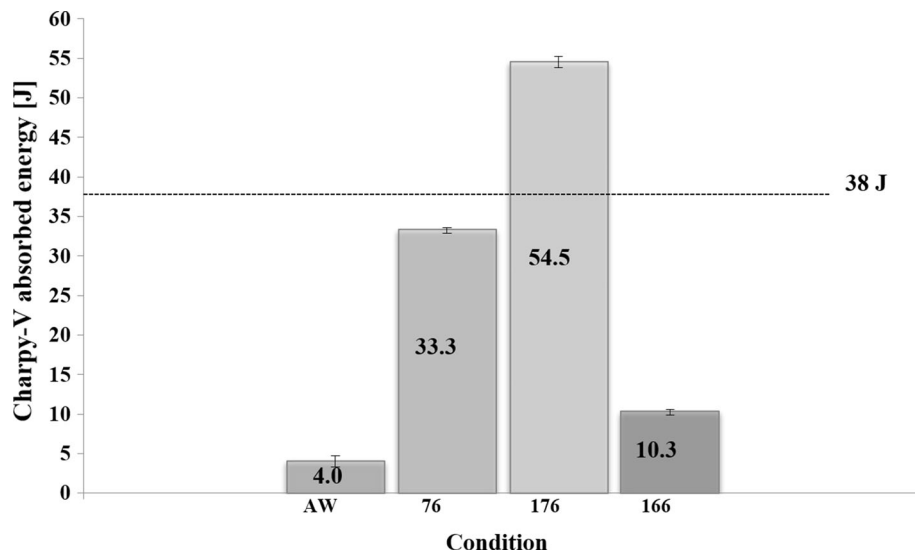


Fig. 15 Effect of PWHT on toughness: Charpy-V at 20 °C values. Individual minimum value required: 38 J (Ref 6)

martensite was enriched in C coming from partially dissolved carbides, which increased its hardness. Minimum values were obtained in the intercritical fine grain HAZ_{AWM} (ICFG-HAZ_{AWM}). In this area, a dual structure coexisted: martensite and tempered martensite (Ref 35).

In the buttered area (which is part of the HAZ_{WJ}), there may have been an intercritical zone between the two beads of the buttering. This zone could have presented a lower hardness (Point 1 in Fig. 11).

Figure 12 shows the microhardness evolution measured in each step of the different PWHTs applied.

In sample 76, the hardness decreased due to the martensite tempering.

In samples 176 and 166, an initial increase in the hardness values was observed as a consequence of the solubilizing treatment. At the high temperatures reached, carbides dissolution took place, increasing C and alloy elements contents in the austenite formed, resulting in the highest martensite hardness.

Regarding the final hardness achieved in the tempering of both 176 and 166 samples, the lower temperature used in the 166 condition could be responsible for the higher hardness values measured (Ref 30).

3.4.2 Hot Tensile Tests. Figure 13 shows the results obtained from HTT and the strain hardening exponent (n) calculated with the Hollomon equation.

It can be observed for each analyzed condition that the strain hardening exponent (n) shows the same behavior. For lower strain rate values, it increases with strain rate to reach a maximum for 1.33E–03 1/s, accordingly with previous results for a P92 steel (Ref 36). The dominance of dynamic recovery is also reflected in the systematic decrease in flow stress and workhardening parameters (n) with decreasing strain rate. The dominance of dynamic recovery at high temperatures has been related to the decrease in dislocation density, formation of well-defined sub-grains rather than poorly defined dislocation tangles/cells and rapid increase in the size of dislocation substructure with increasing temperature (Ref 37, 38).

Then, for higher strain rates, the strain hardening exponent decreases with it. This behavior could be associated with dynamic strain aging (DSA), reported previously for this type of materials, temperatures and strain rates (Ref 36). It has been shown that DSA causes an increased rate of dislocation multiplication and delay in recovery of dislocation structure due to the reduced propensity to cross-slip, leading to uniform distribution of dislocations or poorly defined cell structure (Ref 39-44).

For 76 conditions, the reached values are higher than for the solubilized conditions, and the mentioned effect of n variation is more pronounced.

In Fig. 13, it can also be seen the effect of the initial strain rate on the rest of the mechanical properties in the HTT at 600 °C. Tensile strength tended to increase with the strain rate and reduction in area tended to decrease; elongation did not present a clear trend.

Comparing both solubilized conditions (166 and 176) with similar values of strain hardening exponent, the stress values reached for 166 condition are higher, which could imply a better performance for long service periods. Bueno et al. have proposed a theory that correlates HTT-Creep, from which an approximation to creep parameters can be obtained, considering HTT results (Ref 17-19). The hypotheses on which this reasoning is based are:

- The strain rate imposed in HTT correlates to the minimum creep rate reached in the conventional creep test in similar conditions.
- The ultimate tensile strength (UTS) reached in HTT correlates to the stress applied in a conventional creep test in similar conditions.
- The time at which UTS is reached in HTT correlates to the necessary time to cause the break of the sample in a conventional creep test in similar conditions.

The ultimate tensile strength (UTS) values achieved in HTT have been parameterized according to the Larson–Miller model considering them as stresses applied in creep rupture test (CRT).

The Larson–Miller parameter is given by: $LMP = T \cdot (C + \log t)$, where LMP is the Larson–Miller parameter, T is temperature (K), t is time (h) and C is a constant characteristic of the material, which was obtained from the pattern of the isostress lines creep tests of P92 all-weld metals of similar chemical composition (Ref 44). Table 2 shows the results obtained from the Larson–Miller parameterization using a value of $C = 30$ normally applied for ferritic steels Type 9Cr-1Mo.

In Fig. 14, the results obtained with the Larson–Miller parameterization are shown for all PWHTs conditions. Samples 166 achieved the highest tensile strength in the entire range analyzed, followed by the 176 samples. Nevertheless, considering the LMP at constant temperature as an indicator of time to fracture, a pronounced softening effect is observed in the samples 176 showing a drop in the tensile strength for $LMP > 26 \times 10^3$. It can be said that the hardening mechanisms of the microstructures obtained with this PWHT for this condition fail to retard creep deformation. It is very important to have microstructural obstacles that reduce the minimum creep rate that result in components with longer creep life. Samples 76 presented the lower curve with the lowest loss of tensile strength, but always below that 166 condition. It is reasonable to expect that the microstructural obstacles of

samples 166, which give them higher strength, degrade at a higher rate.

The correlation between HTT and CRT proposed by Bueno et al. (Ref 17, 18) can only be used for extrapolation purposes when is accompanied with creep test data of long time duration to ensure better reliability in these procedures. The results obtained in this work are relevant since there is not information about the application of the proposed methodology for weld metal. In this sense, these results and their analysis can contribute to better understanding of high-temperature mechanical behavior of these types of materials. Moreover, the production of new information about an alternative PWHT applied to gas-shielded flux-cored arc welding is a relevant issue in this area. The validation of these results by conventional creep tests will be carried out in a future work.

3.4.3 Charpy-V Impact Tests. Figure 15 shows the average values of Charpy-V impact tests at 20 °C. As expected, all the PWHTs produced a toughness improvement, compared to the AW condition. The highest toughness value was achieved in sample 176, followed by sample 76 and then sample 166.

Comparing all the analyzed properties, we can observe that sample 176 presented the highest toughness, with the tensile strength and hardness being the lowest and with the elongation and reduction of area being the highest of all the samples. The opposite situation was reached by sample 166, sample 76 being the intermediate one. Comparing microstructures of samples 176 and 166, it can be noticed that the first sample showed low prior austenitic grain size, which could account for better toughness. The prior austenitic grain sizes were not measured; that affirmation came from the visual analysis of Fig. 8(a) and 9(a).

This kind of steel and its weldments are used in different components of steam turbines. For turbine elements, high strength at high temperature is required (Ref 14), then a PWHT 166 would be adequate. For tubes and boiler steam collectors, it is necessary to satisfy requirements of both high tensile strength at high temperature and toughness at room temperature (Ref 6-11), then a PWHT 76 seems to be the more appropriate to give the best combination of both properties.

4. Conclusions

For the all-weld metal deposits submitted to different PWHTs, namely: (1) simple tempering (76), (2) solubilizing + simple tempering (176) and (3) solubilizing + double tempering (166), the following conclusions were obtained:

- Microstructure: sample 166 showed the more uniform precipitate distribution in size and location. In addition, there was an apparent sub-grain generation, obtained from the fine particle accumulation inside the prior austenitic grain.
- Hardness: the heat treatments employed in this work did not modify substantially the final hardness values. Sample 166 showed the highest value.
- Hot tensile property: sample 166 presented the highest tensile strength (consistent with hardness) and the lowest elongation values. The lowest tensile strength was achieved in sample 176 with much higher elongation.
- Toughness: sample 176 results were very much higher than those obtained through conventional simple tempering treatment (sample 76). Sample 166 showed toughness

in the same order of AW sample condition.

- According to HTT data and the Larson–Miller analysis in a conventional creep test, it can be expected to achieve a lower minimum creep rate with samples of solubilizing + double tempering PWHT.

Achieving high levels of toughness, tensile strength and ductility are the purpose for any structural material. Nevertheless, these properties are generally opposed. In this study, sample 166 showed the highest tensile strength and the highest hardness, and the lowest elongation and toughness. Sample 76, subjected to conventional thermal treatment, was in an intermediate situation. Sample 176, on the other hand, reached the highest toughness and elongation, but tensile strength was the lowest.

Acknowledgments

The authors wish to express their gratitude to METRODE PRODUCTS LTD—UK for the design, fabrication and donation of the consumable used, to CONARCO-ESAB Argentina for performing the chemical analysis, to AIR LIQUIDE Argentina for donating gases for welding and to the SCANNING ELECTRON MICROSCOPY LABORATORY OF INTI-Mechanics, Argentina, for facilities for both SEM analysis and Charpy-V tests. They also recognize CONICET, ANPCyT and APUEMFI (National University of Lomas de Zamora), Argentina, for financial support.

References

1. R. Viswanathan, J.F. Henry, J. Tanzosh, G. Stanko, J. Shingledecker, B. Vitalis, and R. Purgert, U.S. Program on Materials Technology for Ultra-Supercritical Coal Power Plants, *J. Mater. Eng. Perform.*, 2005, **14**, p 281–292
2. J. Oñoro, Weld Metal Microstructure Analysis of 9–12% Cr Steels, *Int. J. Press. Vessels Pip.*, 2006, **83**, p 540–545
3. E. Oakey, L.W. Pinder, R. Vanstone, M. Henderson, and S. Osgerby, Review of Status of Advanced Materials for Power Generation Part 4, COAL R224 02/1509, DTI/Pub URN, 2003
4. G. Posch, S. Baumgartner, and M. Fiedler, GMA-Welding of Creep Resistant Steels with Flux Cored Wires (FCAW): Perspectives and Limitations, *Weld. World*, 2009, **53**, p 619–624
5. W. Marshall, Z. Zhang, and G.B. Holloway, Welding Consumables for P92 and T23 Creep Resisting Steels A, in *Fifth International EPRI RRAC Conference*, June 27th, 2002, p. 1–17
6. Z. Zhang, J.C.M. Farrar, and A.M. Barnes, *Weld Metals for P91—Tough Enough*, Metrode Products Limited, U.K. TWI, Ltd., Chertsey, 2002
7. B. Arivazhagan, S. Sundaresan, and M. Kamaraj, A Study on Influence of Shielding Gas Composition on Toughness of Flux-Cored Arc Weld of Modified 9Cr-1Mo (P91) Steel, *J. Mater. Process. Technol.*, 2009, **209**(12–13), p 5245–5253
8. C. Chovet, E. Galand, and B. Leduey, Effect of Various Factors on Toughness in P92 Saw Weld Metal, *Weld. World*, 2013, **52**(7–8), p 18–26
9. Z. Zhang, G. Holloway, and A. Marshall, Properties of T/P92 Steel Weld Metals for Ultra Super Critical (USC) Power Plant, *Weld. World*, 2008, **6**(1), p 1–13
10. H. Wang, H. Zhang, and J. Li, Microstructural Evolution of 9Cr-1Mo Deposited Metal Subjected to Weld Heating, *J. Mater. Process. Technol.*, 2009, **209**(6), p 2803–2811
11. A.C. Chovet, E. Bauné, G. Ehrhart, E. Galand, and G. Liberati, Development of Filler Materials for New 9–12% Cr Martensitic Creep Resistant Steels, in *New Developments on Metallurgy and Applications of High Strength Steels Brazil*, 2008, p. 1–7
12. ISO, *Welding Consumables—Covered Electrodes for Manual Metal Arc Welding of Creep-Resisting Steels—Classification*, ISO 3580:2017, International Organization for Standardization, Geneva, 2017
13. K. Maruyama, K. Sawada, and J. Koike, Strengthening Mechanisms of Creep Resistant Tempered Martensitic Steel, *ISIJ Int.*, 2001, **41**(6), p 641–653
14. P.J. Ennis, The Creep Rupture Behaviour and Steam Oxidation Resistance of P92 Weldments, *Mater. High Temp.*, 2006, **23**(3), p 187–193
15. L.I. Yajiang, W. Juan, Z. Bing, and F. Tao, XRD and TEM Analysis of Microstructure in the Welding Zone of 9Cr-1Mo-V-Nb Heat-Resisting Steel, *Bull. Mater. Sci.*, 2002, **25**(3), p 213–217
16. Y. Yin, R. Faulkner, P. Morris, and P. Clarke, Modelling and Experimental Studies of Alternative Heat Treatments in Steel 92 to Optimise Long Term Stress Rupture Properties, *Energy Mater.*, 2008, **3**(4), p 232–242
17. L.O. Bueno and J.F.R. Sobrinho, Correlation between Creep and Hot Tensile Behaviour for 2.25Cr-1Mo Steel from 500 °C to 700 °C Part 1: An Assessment According to Usual Relations Involving Stress, Temperature, Strain Rate and Rupture Time, *Rev. Mater.*, 2012, **17**(3), p 1098–1108
18. J.A. Moreto, D.B.V. De Castro, L.D.O. Bueno, and H.D.A. Ponte, Correlação de Dados de Tração a Quente e Fluência Para a Liga Kanthal A1, *Rev. Esc. Minas*, 2011, **64**(2), p 181–186
19. P.R. Sreenivasan, Hot-Tensile Data and Creep Properties Derived therefrom for 316L (N) Stainless Steel with Various Nitrogen Contents, *Procedia Eng.*, 2013, **55**, p 82–87
20. American Welding Society, *Specification for Low-Alloy Steel Electrodes for Flux Cored Arc Welding*, ANSI/AWS A5.29/A5.29M:2010, American Welding Society, Miami, 2010
21. ASTM International, *Standard specification for seamless ferritic and austenitic alloy-steel boiler, superheater, and heat-exchanger tubes*, ASTM A213/A213 M-17, ASTM International, West Conshohocken, 2017
22. ASTM International, *Standard specification for seamless ferritic alloy-steel pipe for high-temperature service*, ASTM A335/A335 M-15a, ASTM International, West Conshohocken, 2015
23. ASTM International, *Standard test methods for notched bar impact testing of metallic materials*, ASTM E23-16b, ASTM International, West Conshohocken, 2016
24. R.G. Faulkner, J.A. Williams, E.G. Sanchez, and A.W. Marshall, Influence of Co, Cu and W on Microstructure of 9%Cr Steel Weld Metals, *Mater. Sci. Technol.*, 2003, **19**(3), p 347–354
25. V.T. Paul, S. Saroja, P. Hariharan, A. Rajadurai, and M. Vijayalakshmi, Identification of Microstructural Zones and Thermal Cycles in a Weldment of Modified 9Cr-1Mo Steel, *J. Mater. Sci.*, 2007, **42**(14), p 5700–5713
26. P. Mayr, T.A. Palmer, J.W. Elmer, E.D. Specht, and S.M. Allen, Formation of Delta Ferrite in 9 wt Pct Cr Steel Investigated by In-Situ X-ray Diffraction Using Synchrotron Radiation, *Metall. Mater. Trans. A Phys. Metall. Mater. Sci.*, 2010, **41**(10), p 2462–2465
27. F. Abe and M. Tabuchi, Microstructure and Creep Strength of Welds in Advanced Ferritic Power Plant Steels, *Sci. Technol. Weld. Join.*, 2004, **9**(1), p 22–30
28. K. Kaneko, S. Matsumura, A. Sadakata, K. Fujita, W.J. Moon, S. Ozaki, N. Nishimura, and Y. Tomokiyo, Characterization of Carbides at Different Boundaries of 9Cr-Steel, *Mater. Sci. Eng., A*, 2004, **374**(1–2), p 82–89
29. M. Taneike, F. Abe, and K. Sawada, Creep-Strengthening of Steel at High Temperatures Using Nano-Sized Carbonitride Dispersions, *Nature*, 2003, **424**(6946), p 294–296
30. M.A. Yescas and P.F. Morris, Improved Creep Resistance of Steel 92 by the Use of Modified Heat Treatments, in *ECCC Creep Conference*, 2005
31. K. Tokumo, K. Hanada, R. Uemori, T. Takeda, and K. Itoh, A Complex Carbonitride of Niobium and Vanadium in 9% Cr Ferritic Steel, *Scr. Mater.*, 1991, **25**(4), p 871–876
32. K. Hamada, K. Tokuno, Y. Tomita, H. Mabuchi, and K. Okamoto, Effects of Precipitate Shape on High Temperature Strength of Modified 9Cr-1 Mo Steels, *ISIJ Int.*, 1995, **35**(1), p 86–91
33. M. Hättestrand and H.-O. Andrén, Boron Distribution in 9–12% Chromium Steels, *Mater. Sci. Eng., A*, 1999, **270**(1), p 33–37
34. T. Horiuchi, M. Igarashi, and F. Abe, Improved Utilization of Added B in 9Cr Heat-Resistant Steel Containing W, *ISIJ Int.*, 2002, **42**(Supplement), p S67–S71
35. K. Coleman and W. Newell, P91 and Beyond, *Weld. J. N. Y.*, 2007, **86**, p 29–33

36. G. Sainath, B.K. Choudhary, J. Christopher, E. Isaac Samuel, and M.D. Mathew, Effects of Temperature and Strain Rate on Tensile Stress-Strain and Workhardening Behaviour of P92 Ferritic Steel, *Mater. Sci. Technol.*, 2014, **30**(8), p 911–920
37. D.J. Michel, J. Moteff, and A.J. Lovell, Substructure of Type 316 Stainless Deformed in Slow Tension at Temperatures between 21° and 816 °C, *Acta Metall.*, 1973, **21**, p 1269–1277
38. B.P. Kashyap, K. McTaggart, and K. Tangri, Study on the Substructure Evolution and Flow Behaviour in Type 316L Stainless Steel over the Temperature Range 21–900 °C, *Philos. Mag. A*, 1988, **57**(1), p 97–114
39. J.W. Edington and R.E. Smallman, The Relationship Between Flow Stress and Dislocation in Deformed Vanadium, *Acta Metall.*, 1964, **12**, p 1313–1328
40. D.J. Dingley and D. McLean, Components of Iron, *Acta Metall.*, 1967, **15**, p 885–901
41. A.M. Garde, A.T. Santhanam, and R.E. Reed-Hill, The Significance of Dynamic Strain Aging in Titanium, *Acta Metall.*, 1972, **20**(2), p 215–220
42. J.G. Morris, Dynamic Strain Aging in Aluminum Alloys, *Mater. Sci. Eng.*, 1974, **13**(2), p 101–108
43. S. Okamoto, D.K. Matlock, and G. Krauss, The Transition from Serrated to Non-Serrated Flow in Low-Carbon Martensite at 150 °C, *Scr. Metall. Mater.*, 1991, **25**(1), p 39–44
44. G.B. Holloway, Z. Zhang, and A. Marshall, Properties of T/P92 CrMo Weld Metals for Ultra Super Critical (USC) Power Plant, *Int. J. Microstruct. Mater. Prop.*, 2011, **6**(1/2), p 20–39